Available online at www.sciencedirect.com
SCIENCE DIRECT®
Combustion and Flame 145 (2006) 607–620
Combustion and Flame
www.elsevier.com/locate/combustflame

High-pressure combustion of submillimeter-sized nonane droplets in a low convection environment

J.H. Bae [1], C.T. Avedisian *

Sibley School of Mechanical and Aerospace Engineering, Cornell University, Ithaca, NY 14853-7501, USA

Received 2 July 2004; received in revised form 4 November 2005; accepted 5 December 2005

Available online 13 March 2006

Abstract

An experimental study of droplet combustion of nonane (C_9H_{20}) at elevated pressures burning in air is reported using low gravity and small droplets to promote spherical gas-phase symmetry at pressures up to 30 atm (absolute). The initial droplet diameters range from 0.57 to 0.63 mm and they were ignited by two electrically heated hot wires positioned horizontally on opposite sides of the droplet. The droplet and flame characteristics were recorded by a 16-mm high-speed movie and a high-resolution video camera, respectively. A photodiode is used to measure broadband gray-body emission from the droplet flames and to track its dependence on pressure. Increasing the pressure significantly influences the ability to make quantitative measurements of droplet, soot cloud, and luminous zone diameters. At pressures as low as 2 atm, soot aggregates surrounding the droplet show significant coagulation and agglomeration and at higher pressures the soot cloud completely obscures the droplet, with the result being that the droplet could not be measured. Above 10 atm radiant emissions from hot soot particles are extensive and the resulting flame luminosity further obscures the droplet. Photographs of the luminous zone in subcritical pressures show qualitatively that increasing pressure produces more soot, and the mean photodiode voltage output increases monotonically with pressure. The maximum flame and soot shell diameters shift to later times as pressure increases and the soot shell is located closer to the flame at higher pressure. The soot shell and flame diameter data are correlated by a functional relationship of reduced pressure derived from scaling the drag and thermophoretic forces on aggregates that consolidates all of the data onto a single curve.

Keywords: Droplets; Soot shell; Soot; Droplet combustion; Photodiode; Microgravity

1. Introduction

Much has been written about the high-pressure combustion of liquid fuel droplets and how this poses significant technological challenges [1]. Pressure influences several aspects of the droplet burning process, including flame dynamics, combustion chemistry, evaporation rate, heat-up period, and ignition delay time [2–14]. Conversely, the high-pressure sooting dynamics of droplet flames are not well understood. In this paper we report new experiments which examine the combustion and sooting dynamics of nonane (C_9H_{20}; $P_c = 22.6$ atm; $T_c = 595$ K) droplet flames at pressures from atmospheric, to slightly above the critical pressure, for the particu-

* Corresponding author.
E-mail address: cta2@cornell.edu (C.T. Avedisian).
[1] Current address: Texas Instruments Inc., 529 Pleasant St., Attleboro, MA 02703-0964, USA.

0010-2180/$ – see front matter
doi:10.1016/j.combustflame.2005.12.008

Nomenclature

c_p	gas specific heat
d_p	mean soot aggregate size
D	droplet diameter
D_o	initial droplet diameter
D_f	flame diameter
D_s	soot shell diameter
g	gravitational acceleration (m/s^2)
K	burning rate ($= -dD^2/dt$)
Kn	Knudsen number
P	pressure
P_c	critical pressure
t_f	time to flame extinction
T_c	critical temperature
T_d	temperature at droplet surface
T_s	representative temperature at the soot shell
T_f	flame diameter

Greek symbols

α	gas thermal diffusivity
β	isobaric compressibility
ρ	gas density
ρ_L	liquid density
ν	gas kinematic viscosity
μ	gas dynamic viscosity
Ξ	gas diffusion coefficient

lar configuration of spherical droplet flames. Nonane was selected because it is an appropriate surrogate for examining the influence of pressure on sooting dynamics.

This paper reports the following: qualitative visual observations of the flame structure and soot dynamics as pressure is varied; quantitative measurements for the evolution of effective flame and soot "shell" or "cloud" diameters which cover reduced pressures (P/P_c) from 0.044 to 0.44; and evolution of broadband radiative emission. The measurements and observations are made in an environment in which convection is very low to promote spherical flames. The evolution of outer luminous zone or "flame" diameter and soot cloud diameters are measured at pressures up to 10 atm, and broadband radiative emissions of hot soot particles are measured at pressures up to 30 atm. The diagnostics are high-speed 16-mm movie and video photography, and a photodiode aligned with the droplet to measure broadband emission from the droplet flames. As will be discussed later, the basis for using the output from a photodiode to assess sooting trends is that the gray-body emission arises from the incandescence of hot soot particles within the flame structure surrounding each droplet, and this in turn is indicative of soot formation when certain assumptions are valid. This approach should not, however, be viewed as an absolute measure of soot formation. Nonetheless, it is the next level up from using the image intensity from photographs as a measure of sooting propensities and is a relatively simple approach for application to the low-gravity, high-pressure platform described here.

We found the photodiode output especially useful for differentiating trends for conditions where soot incandescence saturates the movie or video images. The use of a photodiode for broadband emission measurement in droplet combustion experimentation has been previously reported (including for low gravity) to investigate ignition behavior and combustion lifetime in the presence of a strong convective field [15–17].

The initial droplet diameter is in a narrow range—between 0.57 and 0.63 mm—which eliminates the influence of this variable on soot formation [18]. The initial droplet diameter is smaller than examined in previously reported high-pressure droplet combustion studies, yet it is large enough that accurate measurements of the combustion parameters could still be obtained. The ambient gas is room temperature air.

Spherical droplet flames have several important advantages for studying high-pressure effects. They provide a modelable burning condition (e.g., [10,11, 19,20]) by the implied one-dimensional gas-phase transport process; visibility of the soot structure is enhanced compared to combustion in the presence of strong convection because of accumulation of soot aggregates between the droplet and the flame in a shell or cloud structure by the forces acting on them [21,22]; and spherical droplet flames represent the limit condition for convection correlations of the droplet burning rate [23,24] for submodels used in spray codes [25].

High-pressure droplet combustion experimentation in a low convection environment began with the work of Faeth and co-workers [2] and continued into the 1990s with studies by Sato and co-workers [3, 5,8] on both single-component and binary fuel systems. These studies highlighted a number of significant challenges with high-pressure experimentation, especially of the sooting dynamics. Soot formation increases with pressure but the soot shell is not necessarily strengthened at high pressure. Increased soot formation makes aggregates in the shell grow and they can become less stably locked in the shell by the forces acting on them as they get bigger [18]. This fact makes it slightly more challenging to preserve spher-

ical soot dynamics at high pressures. This problem required care in designing the pressure containment to reduce infiltration of extraneous convection into the chamber. Even for pressures near atmospheric, experiments for spherical droplet flames of sooting fuels have shown that the soot shell is exceptionally fragile and easily disturbed by even the smallest convection levels [21,26].

To our knowledge, soot shell dynamics have not been examined for nonane at pressures as high as those reported in the present study. In the experiments we found that flame ignition by spark discharge as used in atmospheric pressure studies (e.g., [18,26–28]) was difficult at high pressure because of the increased spark energy required. This necessitated an alternative design which we based on hot-wire ignition while also striving to maintain some element of ignition symmetry by incorporating two hot wires, one positioned on opposite sides of the droplet.

2. Description of experiment

The combination of using "small" droplets (ranging from 0.57 to 0.63 mm as noted previously) with low gravity produced Rayleigh numbers, $\mathrm{Ra} = gD^3\beta(T_\mathrm{f} - T_\mathrm{d})/\alpha\nu$, of order 10^{-5} to 10^{-6} at 1 atm [27]. Low gravity was created by conducting the experiments in a drop tower facility [28–30] with an experimental time of 1.25 s (the free-fall distance is 7.6 m). This time is long enough to observe the complete burning history for the droplet sizes examined. The drop package is equipped with a drag shield that provides a gravity level of 2×10^{-4} of Earth's gravity during the droplet lifetime.

The general procedure of the experiment is as follows (further details of the hardware and experimental procedures are given in Bae [27]). The combustion chamber is pressurized to the desired pressure. A nonane droplet is then mounted at the intersection of two very small diameter fibers (12 μm diameter). The drop package is then released into free-fall and a short time later two hot wires positioned on opposite sides of the droplet are activated. After the droplet is ignited the hot wires are then rapidly retracted and the burning process is recorded by two cameras providing orthogonal views during the free-fall. In addition to the cameras, broadband gray-body emission by soot oxidation is measured by a photodiode mounted in the pressure chamber close to the droplet as described in the next section.

Fig. 1 shows a schematic of the hardware arrangement including the physical placement of all components. The main components are a combustion chamber, a droplet generation/mounting system, retractable hot-wire igniters, a color CCD camera (Hitachi HV-C20 CCD video camera with a Nikon 135 mm f2.0 lens and 72 mm extension tube), a 16-mm high-speed movie camera (LOCAM II camera operating at 200 fps and shutter speed of 1/450 s with a Nikon 105 mm f2.8 lens, 22-mm extension tube, constant 12-W halogen lamp for back illumination, and Kodak No. 7278 black and white film), and the photodiode. Fig. 1 includes all of the physical dimensions of the camera lenses from the center of the chamber where the droplet is positioned. These are the distances used to obtain the images presented in this study. A cylindrical combustion chamber was designed for a maximum pressure of 48 atm. It was fabricated from 314 stainless with an internal volume of 10.7 liters and four circular optical windows, 5.9 mm diameter, positioned around the periphery to provide orthogonal views of the interior.

A fiber-supported design was used for positioning the test droplets at the location where they could be clearly photographed. The corresponding camera viewing angles are illustrated in Fig. 1b where the "$*$" and "$**$" designations are matched with Fig. 1a (for these viewing angles a "glow" from the flame/fiber interaction was visible which is a useful indicator of flame ignition, flame position, and extinction). It is similar to the previous arrangement [28] except for the physical placement of the support fibers. Two 12-μm-diameter SiC fibers are crossed at 45° to allow direct perpendicular views of the droplet through the chamber ports, and a test droplet is mounted at the intersection of the cross. Crossing two fibers eliminates any tendency of the droplet to slide along the fiber.

Droplets are placed at the intersection of the two fibers by using a piezoelectric droplet generator (with associated reservoir also mounted inside the combustion chamber) to essentially propel one or more droplets to the intersection where the droplet would impinge and stick to the fibers. The desired droplet size is created by successive impingement and coalescence events in a manner similar to that described previously for droplets mounted at the tip of a single fiber [18]. This fiber support arrangement was previously calibrated against combustion of unsupported nonane droplets burning at atmospheric pressure [31]. The evolution of droplet diameter was compared because this is the variable that can be most accurately measured, and the agreement was found to be excellent. For the very small diameter fiber support shown in Fig. 1b, unusual patterns of soot aggregates associated with much thicker fibers [26] were not observed.

Droplets are ignited by hot wires from two circular Kanthal A-1 (33 AWG) wires fashioned into 0.5-mm (i.d.) loops (see Fig. 1b). The two loops are positioned

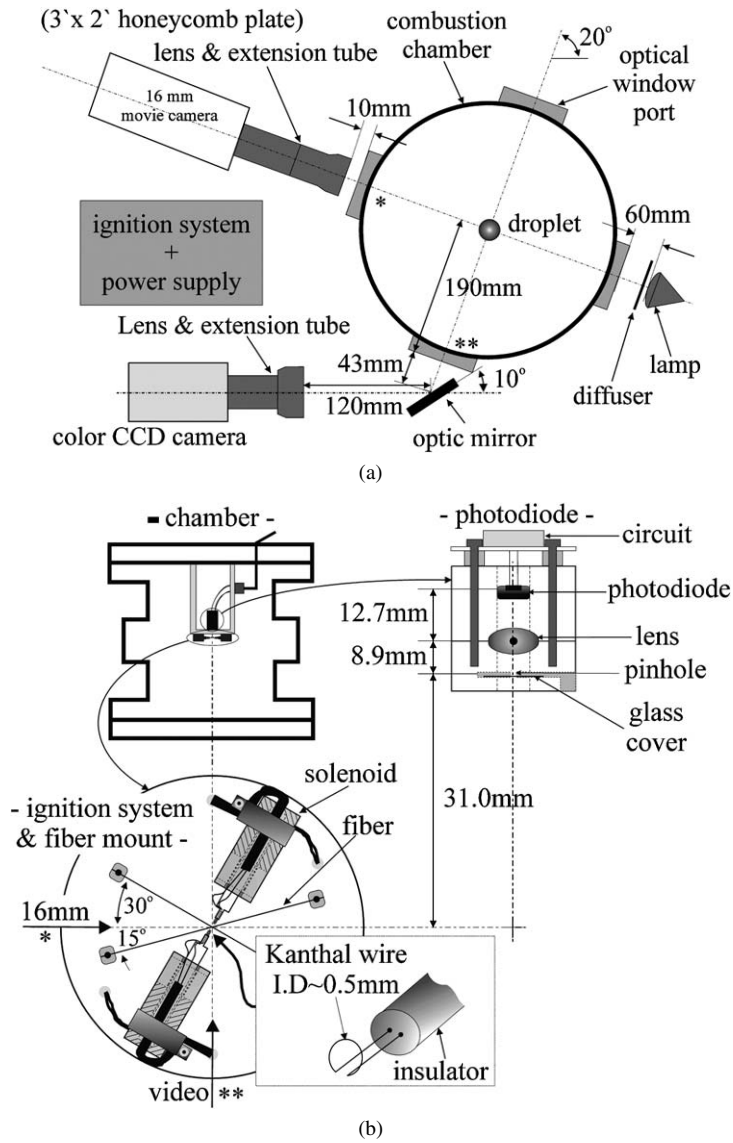

Fig. 1. Schematic of drop package (a) and ignition system and photodiode (b).

horizontally on opposite sides of the droplet to reduce ignition asymmetries. Electrical power (57 W) to the Kanthal wires is initiated 200 ms after the drop package is released. This delay time allows vibrations to dampen in the instrumentation package caused by the physical separation of the instrumentation package from the electromagnet which holds the package in place. The ignition delay ranged from 160 to 210 ms depending on ambient pressure. After ignition the hot wires are quickly retracted (within 10 ms) to allow burning in an unobstructed ambient. A constant electrical power, as well as accurate shape and placement of the hot-wire loops relative to the droplet, was crucial for reliable and repeatable ignition.

Individual images from the video and 16-mm movie cameras were analyzed frame by frame using computer-based software (Media Cybernetics Image-Pro Plus 4.0). The images allow measurements of the effective flame (outer luminous zone) and soot cloud diameters. Droplet diameters could not unfortunately be measured because soot and/or flame luminosity from soot oxidation either partly or completely obscured the droplet at pressures above about 2 atm. We could have compensated for this tendency by reducing the oxygen concentration but doing so would have been counterproductive to studying soot dynamics.

Soot aggregates were collected after burnout from deposits on the fibers and analyzed using a LEO

922 energy filtering transmission electron microscope (TEM), which utilized Koehler illuminations for superior digital image contrast. In this way the aggregates are at maximum size as they correspond to the end of burning. The soot samples were prepared for TEM analysis by first crushing into finer-sized specimens using a mortar and pestle for a uniform specimen thickness over a large area. The soot specimens were attached to a circular copper-grid film with isopropanol solvent, which prevented static force from attracting impurities during measurement.

3. Photodiode output as indicative of soot formation

Semiquantitative information on relative sooting propensities was obtained by using a photodiode to measure broadband radiation arising from radiation emission of hot soot particles. The photodiode (a low capacitance pin photodiode with high near IR responsivity from Pacific Silicon Sensor Inc., Model No. 10-7 with a rise time of 50 ns). Fig. 1b shows the experimental arrangement. The photodiode incorporates a biconvex lens (Newport No. KBX022, f1.0, focal length 12.7 mm) and pinhole located 31 mm above the intersection of the fibers during the entire burning event. The amplified output voltage is collected with a Labview-based data acquisition system at a rate of 1000 samples/s. A protective thin glass cover plate (18×18 mm) was placed over the pinhole.

The physical viewing area covered by the photodetector arrangement shown in Fig. 1b is approximately 700 mm^2 at the plane of the droplet. This area is equivalent to an effective viewing diameter at the droplet plane of 30 mm which is larger than the flame diameter. The practical wavelength range for detection by the photodiode we used is between 350 and 1100 nm.

The interpretation of the photodiode output as a semiquantitative measure of soot formation rests on several assumptions, including that (1) the droplet flame temperature is relatively insensitive to pressure; (2) other forms of radiation (e.g., from CH or C_2 emissions) are negligible compared to broadband emission from incandescent soot aggregates; and (3) all the soot forms within the luminous ball and remains within it during combustion.

The main effect of pressure on soot formation is generally regarded as the flame temperature [32]. If the flame temperature is independent of pressure, changes in soot incandescence as pressure is varied would not then be due to temperature's influence on the radiation field (e.g., the relationship between radiation intensity and temperature from Planck's blackbody radiation law). If aggregates are surrounded by the flame, the flame luminosity is attributed to incandescence of the aggregates (the aggregate temperatures must be at least as high as the soot inception temperature which is of order 1350 K [33]) and not to oxidation of aggregates unless the aggregates are transported through the flame. This effect has been previously observed for unsupported droplets [18,34]. If changes in pressure impart some convective motion to the aggregates that force them through the flame, oxidation of the aggregates could occur which can influence the radiation field, but we have no evidence from our studies that this is the case. If the above conditions are met, it will be reasonable to expect that the voltage output from the photodiode is indicative of the amount of soot formed.

Regarding the flame temperature, detailed simulations of high-pressure spherically symmetric droplet combustion [11] have shown that for subcritical pressures of linear hydrocarbons which is relevant to our situation (e.g., pentane in the simulation) the flame temperature is weakly dependent on pressure, changing less than 100 K from atmospheric to the critical pressure. On this basis we expect that the nonane droplet flame temperature will exhibit a weak dependence on pressure.

The possibility that other constituents of the flame could contribute to the radiation field besides the incandescence of soot aggregates arises from the observed structure of the spherical flame. It consists of a bright yellow core within which the soot shell and aggregates are located, and an outer "blue" zone. This is seen in Fig. 2 (and also in Ref. [31]) which shows selected color flame images of nonane droplets burning at different pressures. The time of the photographs is 230 ms after ignition which is a reference time for which the brightest flame image at 1 atm was observed. The magnification is identical for all photographs in Fig. 2. Specific differences in image intensity are difficult to observe for 2, 4, and 10 atm. Photodiode output helped considerably to differentiate the trends when visual differences were difficult to observe.

The outer blue zone visible at 1 atm in Fig. 2a, and to a lesser extent at elevated pressures, is the result of radiation emitted by CH molecules in the blue/green range of the spectrum. However, CH (and C_2) emissions are primarily line emissions (peaks at wavelengths of 4315 and 5165 Å, respectively). It is reasonable to expect that line radiation will not contribute much energy to broadband emissions from hot soot aggregates. This, together with the flame temperature not being sensitive to pressure as noted above, leaves changes in luminosity and therefore voltage output from the photodiode as being due to variations in soot incandescence and soot formation itself with pressure.

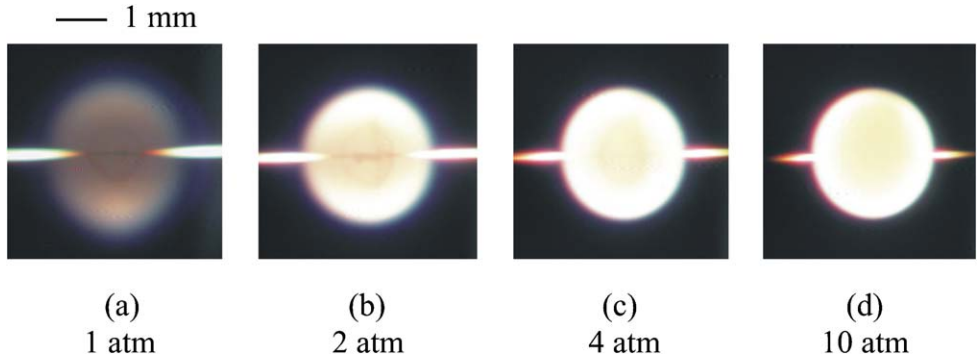

Fig. 2. Non-backlighted color flames of nonane droplets burning at 1 atm (a), 2 atm (b), 4 atm (c), and 10 atm (d) selected at $t \sim 230$ ms. Initial droplet diameters are 0.58 mm. The horizontal bar indicates 1 mm.

When the flame intersects the fiber, the fiber exhibits a "glow" that could influence the radiation field detected by the photodiode which would complicate the interpretation of the diode output as being indicative of the amount of soot present. However, if the flame temperature is independent of pressure, it is reasonable to expect that the radiation field created by the fiber glow is also not pressure dependent. The glow emission should not then bias the photodiode output as pressure is varied.

Because we assumed that the variation of droplet flame temperature with pressure is comparatively weak for our high- (but subcritical) pressure conditions, we look to fuel molecule residence time to explain changes in soot formation with pressure and the radiant emissions from hot soot aggregates that are sensed by the photodiode. Jackson et al. [29] have shown that the residence time of fuel molecules for a spherical droplet flame scales with parameters as

$$t_{\mathrm{res}} \approx \frac{D_{\mathrm{o}}^2 \rho^2 \Xi}{(K\rho_{\mathrm{L}})^2}, \tag{1}$$

where D_{o}, ρ_{L}, ρ, K, and Ξ are the initial droplet diameter, liquid density, vapor density, burning rate, and diffusion coefficient, respectively. As a first approximation, we assume that $\rho\Xi$ is independent of pressure [32], that nonane is an incompressible liquid, and that gas density (ρ) is proportional to pressure (P) (e.g., for an ideal gas). With D_{o} fixed (at about 0.6 mm in the experiments as noted previously), Eq. (1) shows that $t_{\mathrm{res}} \propto P/K^2$. While we could not measure K in our high-pressure experiments from its rigorous definition, $K = -\mathrm{d}(D^2)/\mathrm{d}t$, we defined a "pseudo" burning rate as

$$K = \frac{D_{\mathrm{o}}^2}{t_{\mathrm{f}}}, \tag{2}$$

where t_{f} is the time to disappearance of the flame, or the "extinction time." Equation (2) amounts to drawing a straight line on a graph that plots D^2 with t where $D^2 = D_{\mathrm{o}}^2$ at $t = 0$, and $D^2 = 0$ at $t = t_{\mathrm{f}}$. Table 1 lists measurements of t_{f} which are in most cases average values of two or three experiments [31]. Fig. 3 shows how P/K^2 (units of atm s^2/mm^4) varies with P (atm), which has the expected trend that t_{res} (and soot formation) will increase with pressure. As discussed in the next section, the mean voltage output from the photodiode increases with pressure as well, which is consistent with more soot being formed. As a result of the above, we believe that the photodiode signal is indicative of the amount of soot formed.

Table 1

P (atm)	D_{o} (mm)	t_{f} (s)
1.0	0.58	0.60
2.0	0.57	0.58
3.0	0.56	0.57
4.0	0.59	0.62
10.0	0.58	0.59
15.0	0.56	0.46
20.0	0.59	0.48
25.0	0.62	0.50
30.0	0.61	0.45

4. Discussion of results

Fig. 4 shows a series of backlighted black and white photographs from the 16-mm high-speed movie images that show the development of the soot cloud at pressures of (a) 1 atm, (b) 2 atm, (c) 4 atm, and (d) 10 atm. The backlight intensity was the same for the photographs in Fig. 4 to compare sooting propensities based on image intensity from the high-speed movie images. The image magnification is identical for the photographs. The first image is taken 50 ms after ignition and the last image corresponds to 550 ms which was the burnout time ($t = t_{\mathrm{f}}$) at 1 atm. However, for the higher pressures the last image in Fig. 4

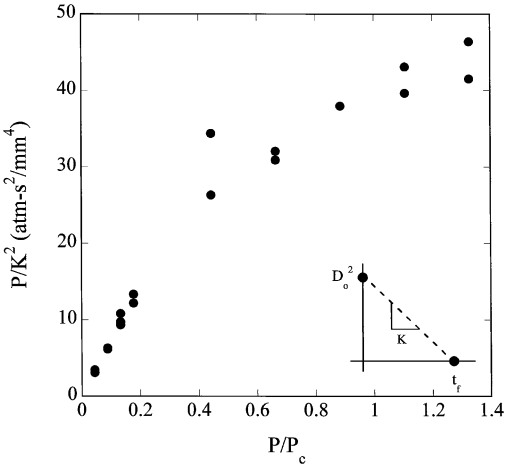

Fig. 3. Variation of residence time (Eq. (1)) with pressure.

does not correspond to burnout. We truncated the sequence to compare the image intensities. Near the end of burning after the flame disappears, a soot cloud remains and more soot seems to be left behind as pressure increases.

At 50 ms for 1 and 2 atm, the droplet is visible through the flame (Figs. 4a and 4b) while at 50 ms for 4 and 10 atm, the flame luminosity is so intense that the droplet is not visible (Figs. 4c and 4d). The droplet comes back into view at 150 ms and 4 atm (Fig. 4c) and eventually becomes obscured by the extensive accumulation of soot as shown for times greater than 250 ms at 4 and 10 atm.

The soot cloud has a distinct and somewhat transparent "shell" structure at 1 atm that gives way to a progressively more dense and less spherical shape as pressure increases, as shown in Figs. 4b–4d. At the highest pressures, the soot shell is so thick and dark that the droplet cannot be viewed through the front face of the cloud. The sooting propensity, being in the order $10 > 4 > 2 > 1$ atm, is consistent with the pressure dependence for the formation of certain radicals (e.g., C_2H_3 and C_3H_3) with pressure [35,36] that lead to precursors for soot. Fig. 4 also shows that pressure appears to exert a progressively greater influence on the sphericity of the soot cloud. This is especially evident at 4 atm later in the burning history (e.g., $t = 450$ ms after ignition).

At very high pressure, increased convection (larger Rayleigh number) produces significant asymmetry in the flame shape as shown in Fig. 5, which is a set of flame-illuminated color photographs of the flame structure at 25 and 30 atm for two different times after ignition. From the definition of the Rayleigh number, and assuming an ideal gas, we can write that

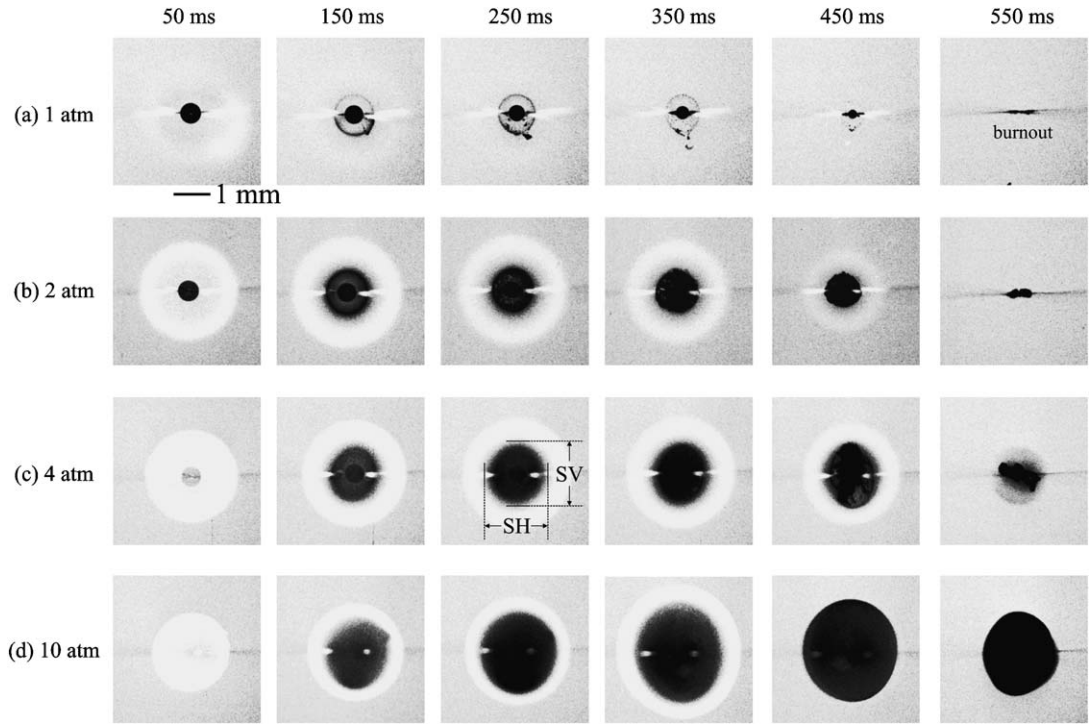

Fig. 4. Backlighted photographs of nonane droplets burning at 1 atm (a), 2 atm (b), 4 atm (c), and 10 atm (d). Time for the photographs after ignition is indicated above series. Initial droplet diameters are (a) 0.57 mm, (b) 0.58 mm, (c) 0.58 mm, and (d) 0.58 mm. The horizontal bar indicates 1 mm.

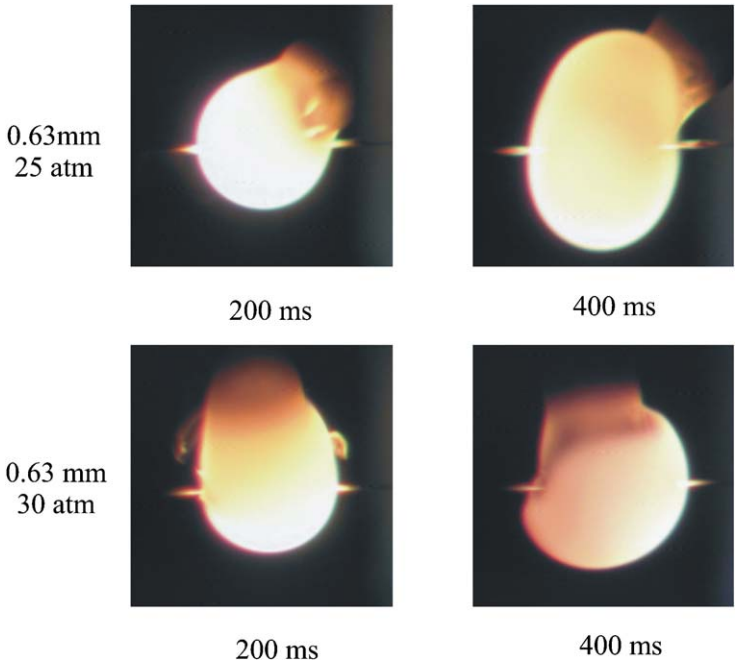

Fig. 5. Selected color photographs (self-illuminated images) showing flame structure at the highest pressures examined.

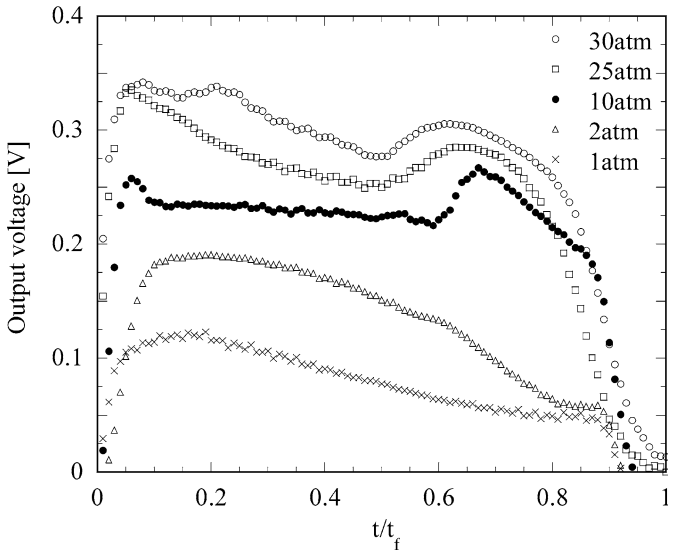

Fig. 6. Evolution of output voltage of the photodiode for different ambient pressures. Initial droplet diameters are as follows: 0.57, 0.58, 0.58, 0.62, and 0.63 mm for 1, 2, 10, 25, and 30 atm, respectively.

$\mathrm{Ra} \sim P^2(D^3 c_{\mathrm{p}} g/k\mu R^2 T_{\mathrm{f}}^2)$. If the term in brackets is independent of pressure, then Ra will increase with pressure and deviations from sphericity are enhanced as pressure increases. This appears to be the case as shown in Fig. 5 which displays photos of flame shapes which are quite nonspherical. While efforts were made to produce a low gravity level to minimize buoyancy-induced flows around the droplet, it is evident that even with a drag shield surrounding the instrumentation package some buoyant effects still appeared to be present at the highest pressures examined.

Fig. 6 shows the evolution of output voltage due to broadband radiation emitted by incandescence of hot soot particles at up to 30 atm. From the photodiode voltage we see differences in Fig. 4 which are not

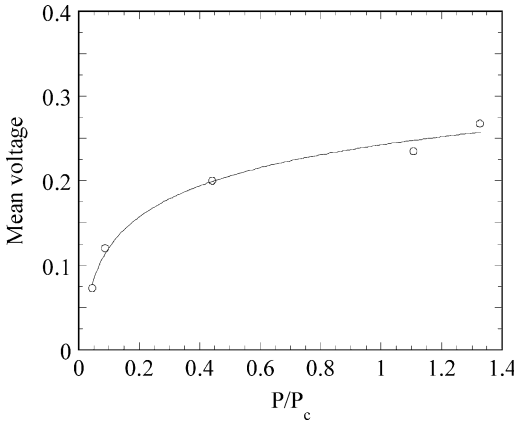

Fig. 7. Evolution of mean voltage of the photodiode for different ambient pressures.

evident from the flame images of Figs. 2 and 4. Varying pressure clearly segregates the emission patterns, with higher pressures clearly showing more broadband emission. This is further illustrated in Fig. 7 in which the variation of mean voltage, $\bar{V}$, is shown with pressure, where $\bar{V}$ is defined as

$$\bar{V} = \frac{1}{t_f} \int_0^{t_f} V(t)\,dt. \tag{3}$$

For a given pressure the evolution of voltage output in Fig. 6 exhibits a rather complicated form that may be explained as follows. Just after ignition, the flame grows and soot develops. The incandescence of the aggregates begins to increase radiant emissions during this early period which is reflected by the voltage increasing for $t/t_f < 0.05$. At the same time, the shell begins to form and thickens. After this early period, and at pressures up to about 10 atm, there is a monotonic decrease of voltage to the end of burning which indicates reduced emissions, perhaps because the shell acts like a radiation shield. At high pressures, however, even though there is a similar decrease in voltage after the initial period, it is followed by a voltage (and emission) increase later in the burning process. This second increase late in the burning process at higher pressure may indicate the dominance of excessive soot formation and incandescence at high pressure that overrides the tendency of the shell to act as a radiation shield. Complicating this explanation is the effect of residence time on soot formation, which is influenced by both droplet diameter and pressure. Soot formation decreases as droplet diameter decreases and this will favor a lower diode voltage as burning proceeds. At the same time, as pressure increases the residence time increases as discussed previously (Eq. (1)) which in turn increases emissions and is broadly consistent with a second peak forming as indicated by the data in Fig. 6.

Fig. 8 shows TEM images of nonane soot aggregates at selected pressures (1 atm (a), 10 atm (b), 20 atm (c), and 30 atm (d)); the dark structures in the background shown in Figs. 8a and 8b are the copper-grid film to support soot particles. Again, and as noted previously, the aggregates shown in Fig. 8 correspond to the largest size because they were obtained at the end of burning. The soot aggregates are interconnected and individual elements appear to be of a somewhat spherical shape, which is similar to images reported in other studies under terrestrial and low-gravity conditions [37–39]. Interestingly, aggregate size (d_p) is influenced by ambient pressure as shown in Fig. 9 which is based on measurements from images similar to those shown in Fig. 8 and, for the present data, are considered to represent the largest sizes produced in the nonane flame. For comparison we also show data reproduced from Kadota et al. [38] at Earth's normal gravity. The fuel examined by Kadota is different, but as noted by Dobbins et al. [40] and Palmer and Cullis [41], soot properties tend to be independent of fuel type and the trends in Fig. 9 would be essentially the same. The solid line through the data in Fig. 9 is drawn to suggest the trend of pressure. The displacement between the two data sets is the result of different transport conditions and residence times between the two experimental conditions. The linear relationship in Fig. 9 on the logarithmic scale suggests that $d_p \sim \ln(P/P_c)$, which we will return to shortly in an attempt to develop a correlation of our measurements. Fig. 9 shows the aggregate sizes formed under terrestrial conditions are clearly smaller than at low gravity because of the smaller residence time at normal gravity from strong convection compared to low gravity.

The average aggregate (and largest) diameter at 1 atm is about 60 nm as shown in Fig. 9 which is also similar to measurements of very different fuels (e.g., JP8 [39]). At 30 atm the aggregate size is about is 190 nm. Soot precursor diameters for diffusion flames at normal gravity were previously reported to be in the range of 10 to 40 nm [37]. The larger diameter of soot aggregates in the present study is a result of the longer residence times at low gravity and high pressure, and the fact that the aggregates are sampled at the end of the burning process as noted previously.

Fig. 10 shows the evolution of D_f and D_s ($D_f < D_s$) which are both scaled with the initial droplet diameter, D_o, since instantaneous droplet diameter (D) was not measured as noted previously. Flame and soot shell diameters were measured from non-backlighted video and backlighted black and white photographs such as illustrated in Fig. 4. At pressures higher than 10 atm, significant deviations from sphericity

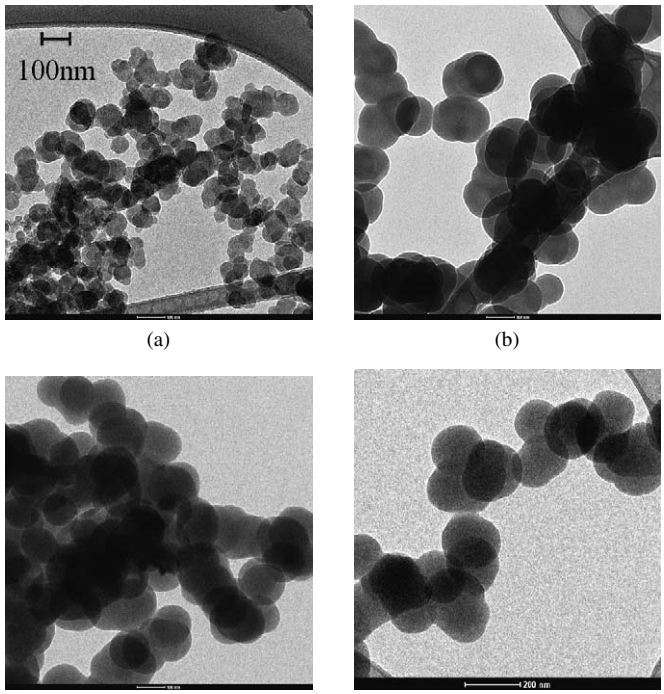

Fig. 8. Transmission electron microscope (TEM) photographs of soot aggregates collected from nonane droplets burning at 1 atm (a), 10 atm (b), 20 atm (c), and 30 atm (d).

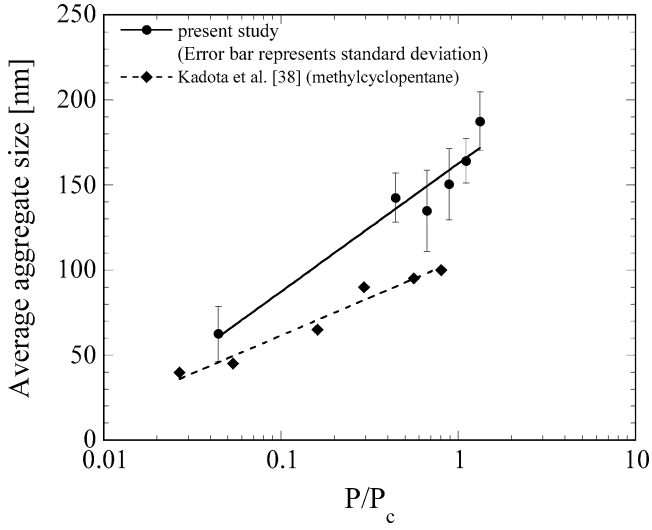

Fig. 9. Relation between soot aggregate size and reduced pressure.

were observed as measured by the aspect ratio of the flame and soot cloud (i.e., symbols "FH" and "FV" in Fig. 10). Quantitative measurements of D_f and D_s in Fig. 10 are reported only for $0.90 < \text{FH/FV: SH/SV} < 1.1$. The gap in the data for D_s early in the burning history is the result of the delay period of soot formation; later in the process severe buildup of soot and distortion of the shell symmetry (i.e., aspect ratio greater than 1.1) made it impractical to report meaningful measurements. Measurements of D_s could not be made over the same range of times that D_f could be measured. For example, at 1 atm (Fig. 10a), data for D_f are shown for $0.05 < t/t_f < 0.9$ while D_s could only be measured for $0.2 < t/t_f < 0.67$. We re-

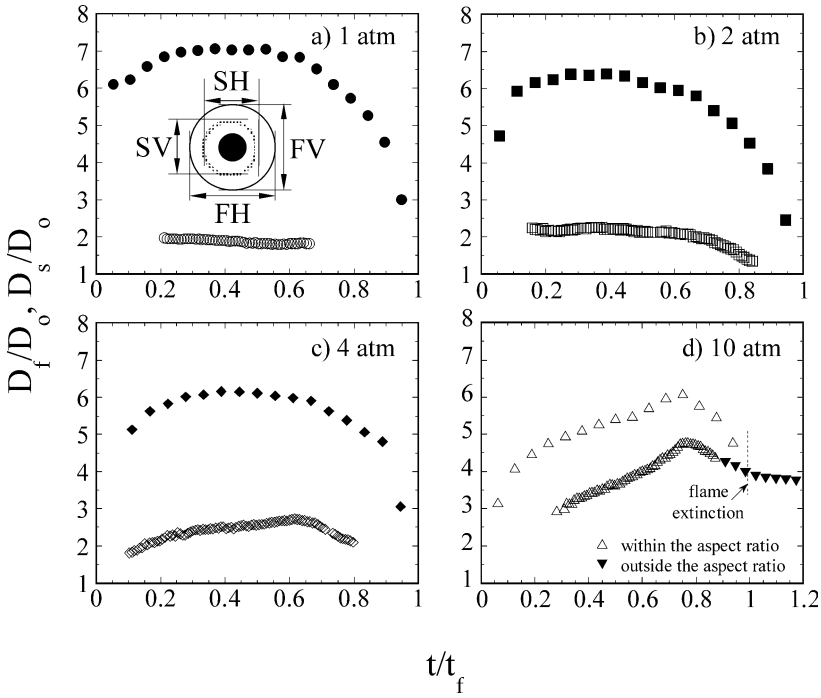

Fig. 10. Evolution of flame and soot shell diameters, expressed as a flame "ratio" and soot "ratio," for different ambient pressures. Initial droplet diameters are identical to those in Fig. 4.

laxed the above restriction on aspect ratio at 10 atm to illustrate the interesting soot shell dynamic at high pressure (data distinguished by "▼" in Fig. 10d). After burnout, the soot shell at 10 atm did not shrink completely but rather appeared to form a hard shell or "crust"—note the tail of the D_s data in Fig. 10d.

At high pressure D_s increases with time and reaches a maximum (Figs. 10c and 10d) and then gradually decreases at the end of combustion. This trend contrasts with the near time independence of D_s (and somewhat D_f as well) at low pressures as shown in Figs. 10a and 10b. D_f is time dependent over a larger portion of the burning history at high pressures than low pressures as shown by comparing Fig. 10a with Fig. 10d. The peak in D_f shown in Figs. 10c and 10d is consistent with the experimental studies of Sato et al. [3]. Since D_s tracks with D_f, the soot shell diameter also exhibits a peak as shown in Figs. 10c and 10d. The peak of D_s and D_f shifts to later times as pressure increases.

For all pressures investigated D_s tracks reasonably well with D_f for a given pressure, and as shown in Fig. 11a they are in a constant ratio and independent of time at a given pressure. The soot shell tracks with the flame because the forces on the aggregates which define D_s depend on D_f and the droplet diameter. On the other hand, as pressure increases the soot shell moves toward the flame as shown in Fig. 11b which indicates a faster rate of change of D_s compared to D_f with increasing pressure.

There is no theory to predict the pressure dependence of the flame and soot cloud diameter. As a result, we correlate these parameters using our measured data. The correlation is based on a scaling of the forces (or equivalently the velocities) which act on the aggregates, with the soot shell corresponding to the radial position where the forces balance. The two principle forces are the Stefan drag due to the evaporation-induced velocity which acts on aggregates toward the flame, and the thermophoretic force due to the temperature gradient between the droplet and flame which acts toward the droplet. We assume diffusiophoresis and other effects are negligible for the present purposes. We are only interested here in an order of magnitude analysis to identify a scaling to correlate the data and these assumptions and those which follow will allow us to do that.

The soot shell diameter corresponds to the condition

$$\bar{F}_T = \bar{F}_D, \tag{4}$$

where $\bar{F}_T$ and $\bar{F}_D$ are nondimensional thermophoretic and drag forces, respectively. Jackson et al. [29] present equations for $\bar{F}_T$ and $\bar{F}_D$ as

$$\bar{F}_D = G \tag{5}$$

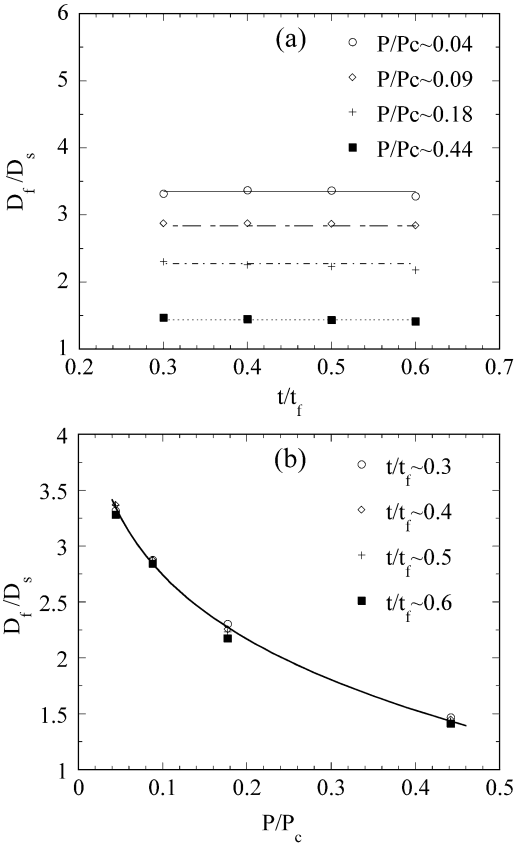

Fig. 11. Ratio of flame diameter to soot shell diameter with respect to time (a) and pressure (b).

and

$$\bar{F}_{\mathrm{T}} = \frac{D\mu}{K\rho_{\mathrm{l}}}\frac{1}{T}\frac{\partial T}{\partial r}H, \tag{6}$$

where G and H are functions of the Knudsen number (Kn) based on the aggregate radius ($\mathrm{Kn} = d_{\mathrm{p}}/\lambda$ where λ is the mean free path) and the coefficients associated with momentum exchange, thermal slip, and a temperature jump at the interface. Scaling the derivative as $\partial T/\partial r \sim (T_{\mathrm{f}} - T_{\mathrm{s}})/(D_{\mathrm{f}} - D_{\mathrm{s}})$, taking $T \sim T_{\mathrm{f}}$, and assuming that K relates to variables as it will from the quasi-steady theory of droplet burning [32], $K \sim (k/\rho_{\mathrm{l}}C_{\mathrm{p}})\ln(1+B)$, where B is the transfer number (our results are not indicative of a quasi-steady burning process but for scaling purposes we nonetheless use this relationship to illustrate how K might be expected to depend on variables), Eq. (4) can be rearranged to

$$\frac{D_{\mathrm{f}}}{D_{\mathrm{s}}} = 1 + f(t,P)\left(\frac{D_{\mathrm{s}}}{D}\right)^{-1}, \tag{7}$$

where

$$f(t,P) = \frac{\mathrm{Pr}}{\ln(1+B)}\left(1 - \frac{T_{\mathrm{s}}}{T_{\mathrm{f}}}\right)\frac{H}{G}. \tag{8}$$

As noted previously, our data show that $D_{\mathrm{f}}/D_{\mathrm{s}}$ is independent of time (see Fig. 11a). This means that $f(t,P)(D_{\mathrm{s}}/D)^{-1}$ is independent of time. Data for the soot "ratio" (D_{s}/D) at atmospheric pressure show a weak time dependence [18,31] so that the time dependence of f to compensate would then come through T_{s}, T_{f}, and d_{p}. Except in the initial transient period, T_{s} and T_{f} may be considered constant in the quasi-steady limit. Aggregates grow and their size depends on time. We assume that the time dependence of d_{p} is not significant in its contribution to H and G, and hence f. The predicted variation of soot shell diameter [42] with mean aggregate size for a given pressure is also expected to be small for the aggregate sizes shown in Fig. 9. This leaves pressure as an influence. The Prandtl number (Pr) will not have a strong dependence on pressure for the pressure range of our data. T_{s}, T_{f}, and D_{s}/D should depend on pressure but since we are interested in using Eq. (7) as a correlating equation, we will for the present purposes absorb the pressure dependence of T_{s} and T_{f} in the soot ratio. We write Eq. (7) in a more general form

$$\frac{D_{\mathrm{f}}}{D_{\mathrm{s}}} = C_1 + C_2\left(\frac{D_{\mathrm{s}}}{D}\right)^{-1}, \tag{9}$$

where C_1 and C_2 are constants and, again, the pressure dependence of $D_{\mathrm{f}}/D_{\mathrm{s}}$ is carried in the soot ratio.

To determine an appropriate functional form of pressure for D_{s}/D, we assume that growth and expansion of the soot shell will be accompanied by an increase of mean soot aggregate size, d_{p}, and that $D_{\mathrm{s}}/D \propto d_{\mathrm{p}}$. Our measurements of d_{p} for nonane (Fig. 9 shows data believed to be for the largest aggregates as noted previously) increase with pressure. The data fit a logarithmic function of P/P_{c} in the form $d_{\mathrm{p}} \propto \ln(C_3 P/P_{\mathrm{c}})$. Therefore, a slightly more generalized form of Eq. (9) is

$$\frac{D_{\mathrm{f}}}{D_{\mathrm{s}}} = C_1 + C_2\frac{1}{\ln(C_3 P/P_{\mathrm{c}})}. \tag{10}$$

Fig. 11b uses this correlation to provide a best fit of the data. Values of $C_1 = 13.6$, $C_2 = 150$, and $C_3 = 10^{-5}$ which worked well for the reduced pressure range covered by the data, $0.044 < P/P_{\mathrm{c}} < 0.44$. It is important to note that these coefficients should not be used outside of this reduced pressure range because $D_{\mathrm{f}}/D_{\mathrm{s}} < 1$ is an impossible condition (which is reached for $P/P_{\mathrm{c}} > 0.6758$ using these coefficients).

As a final point we place Eq. (9) in the context of a scaling relationship for D, D_{s}, and D_{f} that was previously developed for jet fuels in terms of the fraction of the total burning time, t/t_{b} [31]. We rewrite the correlation of [31] in the form

$$\left(\frac{D_{\mathrm{f}} - D_{\mathrm{s}}}{D_{\mathrm{s}} - D}\right) = -C_2\left(\frac{t}{t_{\mathrm{b}}}\right)^{n}, \tag{11}$$

where $t_b \sim t_f$ and we have put the constant as $-C_2$. Pressure does not explicitly appear as a parameter in Eq. (11) because the data for Eq. (11) [31] were obtained at a single pressure (i.e., normal atmospheric pressure). Close examination of those data also show that at atmospheric pressure D_f/D_s is not strongly time dependent. The time function in Eq. (11) essentially disappears for the data of [31] and Eq. (11) can be written as

$$\frac{D_f}{D_s} = (1 - C_2) + C_2\left(\frac{D_s}{D}\right)^{-1}. \tag{12}$$

Equation (12) is in the form of Eq. (9) if $1 - C_2$ is replaced by a new constant, C_1, which we are allowed to do in the context of scale analysis.

5. Conclusions

We report the first observations of development of the soot cloud or shell for nonane droplet combustion at high pressures. The experimental observations show that soot shells of reasonable sphericity exist at pressures up to about 10 atm. At the highest pressure studied, 30 atm, droplet flames are noticeably nonspherical because increased convection levels and formation progressively obscure droplet visibility as pressure was increased. Broadband emission from incandescence of hot soot aggregates increases with pressure as evidenced by the voltage output from the photodiode increasing with pressure. The increase of soot formation with pressure is explained by the influence of pressure on residence time. A correlation for the soot shell diameter covers the range $0.044 \leqslant P/P_c \leqslant 0.44$ that consolidates the evolution of flame and soot shell diameter onto a single curve.

Acknowledgments

The authors acknowledge many helpful discussions with Professor Richard A. Dobbins of Brown University. The assistance of Messrs. Colby Farris, John Kim, and Katherine Lee with some of the experiments is also gratefully acknowledged. We thank the National Aeronautics and Space Administration for supporting this work through Grant NAG 3-2224 with Dr. Daniel Dietrich as Project Monitor and Dr. Merrill King as Program Director.

References

[1] S.D. Givler, J. Abraham, J. Prog. Energy Combust. Sci. 22 (1996) 1–28.
[2] G.M. Faeth, D.P. Dominicis, J.F. Tulpinsky, D.R. Olson, Proc. Combust. Inst. 12 (1969) 9–18.
[3] J. Sato, M. Tsue, M. Niwa, M. Kono, Combust. Flame 82 (1990) 142–150.
[4] C. Chauveau, X. Chesneau, I. Gökalp, in: 31st Aerospace Sciences Meeting & Exhibit Reno, NV, 1993, AIAA 93-0824.
[5] M. Mikami, K. Kono, J. Sato, D.L. Dietrich, F.A. Williams, Combust. Sci. Technol. 90 (1993) 111–123.
[6] B. Vieille, C. Chauveau, X. Chesneau, A. Odeïde, I. Gökalp, Proc. Combust. Inst. 26 (1996) 1259–1265.
[7] H. Nomura, Y. Ujiie, H.J. Rath, J. Sato, M. Kono, Proc. Combust. Inst. 26 (1996) 1267–1273.
[8] K. Okai, M. Tsue, M. Kono, M. Mikami, J. Sato, D.L. Dietrich, F.A. Williams, Proc. Combust. Inst. 27 (1998) 2651–2657.
[9] H. Kobayashi, J. Park, T. Iwahashi, T. Niioka, Proc. Combust. Inst. 29 (2002) 2603–2610.
[10] I. Aharon, B.D. Shaw, Combust. Flame 113 (1998) 507–518.
[11] J.S. Shuen, V. Yang, C.C. Hsiao, Combust. Flame 89 (1992) 299–319.
[12] C. Chauveau, X. Chesneau, B. Vieille, A. Odeïde, I. Gökalp, Materials and Fluids under Low Gravity, Lecture Notes in Physics, vol. 464, 1996, pp. 415–424.
[13] T. Kadota, K. Satoh, D. Segawa, J. Sato, Y. Marutani, Proc. Combust. Inst. 27 (1998) 2595–2601.
[14] K. Okai, Y. Ono, O. Moriue, H. Kato, M. Tsue, M. Kono, J. Sato, D.L. Dietrich, F.A. Williams, JSME Int. J. Ser. B 43 (3) (2000) 485–490.
[15] G.J. Green, T.Y. Yan, in: Proceedings of the 23rd Intersociety Energy Conversion Engineering Conference, ASME, New York, 1988, pp. 291–296.
[16] R. Nakanishi, H. Kobayashi, S. Kato, T. Niioka, Proc. Combust. Inst. 25 (1994) 447–453.
[17] T. Kadota, H. Hiroyasu, Proc. Combust. Inst. 18 (1981) 275–282.
[18] G.S. Jackson, C.T. Avedisian, Proc. R. Soc. London A 446 (1994) 255–276.
[19] J. Bellan, Prog. Energy Combust. Sci. 26 (2000) 329–366.
[20] J. Daou, P. Haldenwang, C. Nicoli, Combust. Flame 101 (1995) 153–169.
[21] C.T. Avedisian, in: Physical and Chemical Aspects of Combustion, Gordon & Breach, Amsterdam, 1997, Chap. 6, pp. 135–160.
[22] G. Ben-dor, T. Elperin, B. Krasovitov, Proc. R. Soc. London A 459 (2003) 677–703.
[23] W.A. Sirignano, Fluid Dynamics and Transport of Droplets and Sprays, Cambridge Univ. Press, Cambridge, UK, 1999, pp. 23–25.
[24] S.S. Sadhal, P.S. Ayyaswamy, J.N. Chung, Transport Phenomena with Drops and Bubbles, Springer-Verlag, New York, 1997, pp. 101–102.
[25] A.A. Amsden, LANL Report LA-13313-MS, July 1997.
[26] C.T. Avedisian, G.S. Jackson, J. Prop. Power 16 (6) (2000) 974–979.
[27] J.H. Bae, Ph.D. thesis, Sibley School of Mechanical and Aerospace Engineering, Cornell University (2005).
[28] C.T. Avedisian, B.J. Callahan, Proc. Combust. Inst. 28 (2000) 991–997.
[29] G.S. Jackson, C.T. Avedisian, J.C. Yang, Int. J. Heat Mass Transfer 35 (1992) 2017–2033.
[30] C.T. Avedisian, J.C. Yang, C.H. Wang, Proc. R. Soc. London A 420 (1988) 183–200.

[31] J.H. Bae, C.T. Avedisian, Combust. Flame 137 (2004) 148–162.
[32] I. Glassman, Combustion, third ed., Academic Press, New York, 2002, pp. 133, 420.
[33] R.A. Dobbins, Combust. Flame 130 (2002) 204–214.
[34] G.S. Jackson, C.T. Avedisian, Int. J. Heat Mass Transfer 41 (1998) 2503–2515.
[35] W. Tsang, NIST, personal communication, December 1, 2003.
[36] A. Yozgatligil, M.Y. Choi, A. Kazakov, F.L. Dryer, S.L. Manzello, R. Dobashi, in: 41st Aerospace Sciences Meeting & Exhibit, Reno, NV, 2003, AIAA Paper No. 2003-1147.
[37] C.M. Megaridis, R.A. Dobbins, Combust. Sci. Technol. 66 (1989) 1–16.
[38] T. Kadota, H. Hiroyasu, A. Farazandehmehr, Combust. Flame 29 (1977) 67–75.
[39] J.H. Bae, C.T. Avedisian, Environ. Sci. Technol. 39 (2005) 8008–8013.
[40] R.A. Dobbins, R.A. Fletcher, H.C. Chang, Combust. Flame 115 (1998) 285–298.
[41] H.B. Palmer, C.F. Cullis, in: P.L. Walker Jr., P.A. Thrower (Eds.), Chemistry and Physics of Carbon, vol. 1, Dekker, New York, 1965, pp. 265–325.
[42] G.S. Jackson, C.T. Avedisian, Combust. Sci. Technol. 115 (1996) 127–147.